INTERNATIONAL JOURNAL FOR NUMERICAL METHODS IN FLUIDS
Int. J. Numer. Meth. Fluids 2008; **57**:475–493
Published online 19 September 2007 in Wiley InterScience (www.interscience.wiley.com). DOI: 10.1002/fld.1590

Computational fluid dynamics of stented intracranial aneurysms using adaptive embedded unstructured grids

S. Appanaboyina[1], F. Mut[1], R. Löhner[1], C. M. Putman[2] and J. R. Cebral[1,*,†]

[1]*Center for Computational Fluid Dynamics, George Mason University, 4400 University Drive, Fairfax, VA 22030, U.S.A.*
[2]*Interventional Neuroradiology, Inova Fairfax Hospital, 3300 Gallows Road, Falls Church, VA 22042, U.S.A.*

SUMMARY

Recently, there has been increased interest in the use of stents as flow diverters in the endovascular treatment of cerebral aneurysms as an alternative to surgical clipping or endovascular embolization with coils. The aim of aneurysm stenting is to block the flow into the aneurysm in order to clot the blood inside the aneurysm and effectively isolate it from the circulation and prevent bleeding from the aneurysm. A hybrid meshing approach that combines body-fitted grids for the vessels and adaptive embedded grids for the stents is proposed and analyzed. This strategy simplifies considerably the geometry modeling problem and allows accurate patient-specific hemodynamic simulations with endovascular devices. This approach is compared with the traditional body-fitted approach in the case of the flow around a circular cylinder at representative Reynolds number and an idealized aneurysm model with a stent. A novel technique to map different stent designs to a given patient-specific anatomical model is presented. The methodology is demonstrated on a patient-specific hemodynamic model of an aneurysm of the internal carotid artery constructed from a 3D rotational angiogram and stented with two different stent designs. The results show that the methodology can be successfully used to model patient-specific anatomies with different stents thereby making it possible to explore different stent designs. Copyright © 2007 John Wiley & Sons, Ltd.

Received 27 October 2006; Revised 6 July 2007; Accepted 9 July 2007

KEY WORDS: computational fluid dynamics; adaptive embedded unstructured grids; cerebral aneurysms; stenting

1. INTRODUCTION

Cerebral aneurysms are pathological dilations of the cerebral arteries, most commonly found at arterial bifurcations in or near the circle of Willis. The mechanisms responsible for the initiation, evolution and rupture of cerebral aneurysms are not well understood. This is a multi-factorial

*Correspondence to: Juan R. Cebral, Center for Computational Fluid Dynamics, George Mason University, 4400 University Drive, Fairfax, VA 22030, U.S.A.
†E-mail: jcebral@gmu.edu

Contract/grant sponsor: Philips Medical Systems

Copyright © 2007 John Wiley & Sons, Ltd.

problem involving: (a) hemodynamics, (b) wall biomechanics, (c) extravascular environment, (d) aneurysm morphology, (e) genetics, and (f) other clinical and epidemiological factors. However, it is thought that hemodynamic characteristics such as wall shear stress, vorticity, jetting, recirculation and pressure fluctuation play an important role in the inception and later development of aneurysms.

Rupture of these aneurysms results in subarachnoid hemorrhage which is often fatal [1–7]. Intracranial aneurysms are treated either using surgery or endovascular procedures [8]. Surgery involves placing a metallic clip across the neck of the aneurysm thereby separating it from the circulation, whereas in the case of endovascular procedures intravascular devices such as coils and/or stents are placed inside the aneurysm or in the parent vessel to limit the blood flow into the sac promoting thrombus formation. In these cases, the aim of the procedure is to completely clot the aneurysm effectively isolating it from the arterial circulation and thus prevent aneurysm rupture and bleeding into the brain. Surgical clipping is not always the preferred choice because of the high risks involved and often it is very difficult or nearly impossible to clip an aneurysm. Coil embolization is the most commonly used endovascular method to treat cerebral aneurysms. This involves filling the aneurysm with platinum coils to stop the flow of blood into the sac. However, this procedure is prone to complications such as coil compaction followed by re-growth of the aneurysm or the formation of a secondary aneurysm. As a result many patients need to be re-treated. Wide neck or fusiform aneurysms fall under the category of aneurysms that are problematic or in some cases impossible to coil. In cases like these a stent which is an expandable mesh made up of surgical grade metal is put in the parent vessel across the neck of the aneurysm to hold the coils inside the sac. Currently, there is considerable interest in the use of stents as flow diverters. If properly designed, stents without the use of coils can be used to deviate the flow of blood away from the aneurysm, thereby promoting thrombus formation and reducing the risk of bleeding [9–11].

Extensive studies have been conducted using idealized *in vitro* and numerical models to study the flow alterations inside the aneurysms caused by the presence of stents [12–15]. These idealized models cannot be directly used for relating the patient-specific hemodynamics to clinical events or planning endovascular stenting procedures because they fail to replicate the anatomy of the human arteries. In contrast, personalized or patient-specific models created from medical images provide an attractive alternative to study the flow alterations caused by the stenting procedures [16–20]. However, the main difficulty lies in the construction of acceptable computational grids inside the blood vessel and around these devices.

In this paper an adaptive unstructured embedded grid approach for modeling blood flow past stents [21, 22] is analyzed. This technique uses a hybrid approach wherein the vessel walls are treated with body-fitted unstructured grids and the stents are embedded in this grid. Adaptive mesh refinement is used to increase the mesh resolution around the device. This technique is compared with the body-fitted approach and with experimental data reported in the literature. An algorithm to map a particular stent to a patient-specific vascular model is presented. Finally, the methodology is demonstrated in a patient-specific model of an internal carotid artery aneurysm constructed from a 3D angiogram and treated with different stents.

2. METHODS

2.1. Vascular modeling

In this paper both idealized and realistic or patient-specific anatomical models are used to assess the proposed methodology. Idealized vascular models are constructed by combining basic shapes such

Copyright © 2007 John Wiley & Sons, Ltd.

DOI: 10.1002/fld

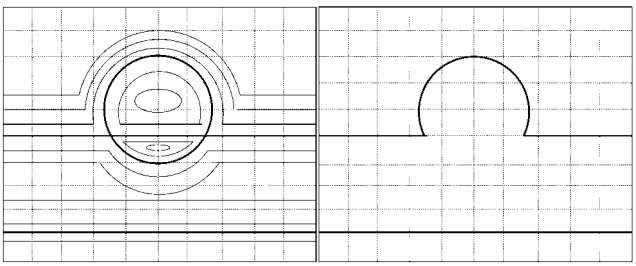

Figure 1. Contours of the distance-to-surface function (left) and the merged object (right).

as cylinders and spheres. Once these shapes have been triangulated, an adaptive surface-merging algorithm is used to fuse them [23]. The basic idea of this algorithm is to construct a background grid covering all the surfaces to merge and compute the signed distance from each point of this grid to the closest surface triangulation. Then, the fused surface is recovered as the zero-level iso-surface of this distance map. Adaptive grid refinement is used in order to increase the resolution close to the surfaces. The iso-surface is extracted with an advancing tetrahedra algorithm [24]. Figure 1 illustrates schematically the contours of the distance-to-surface function, where the zero-level contour is the merged object. Idealized models of blood vessels and aneurysms can be constructed effortlessly with this component-based approach. Although the final result is an idealized geometrical model, it does not contain sharp edges typically encountered when creating models with a computer-aided design (CAD) system. We are well aware that some *in vitro* models, as well as many mechanical devices have sharp corners. However, from the radiological data gathered so far we have not been able to discern any sharp corners for arteries, thus making this a viable approach.

The patient-specific models are constructed from anatomical images such as 3D rotational angiography (3DRA) using a previously developed methodology [19]. Briefly, the images are first filtered using a combination of blurring and sharpening operations in order to reduce the noise. This is followed by a region growing segmentation and an iso-surface extraction. Again, the iso-surface extraction is carried out using an advancing tetrahedra algorithm. The extracted iso-surface is allowed to deform under the action of internal smoothing forces and external forces obtained from the gradients of the original un-processed image. This deformable model tends to make the surface coincide with the vessel boundaries detected in the image. The surface is then smoothed using a non-shrinking algorithm and the vessels are interactively truncated perpendicularly to their axis.

The final step is the generation of a finite element grid. This is achieved with an advancing front method. First, the surface of the model is re-triangulated and then the volume is filled with tetrahedral elements [25, 26]. The size of the elements is chosen in such a way that every vessel has at least a given minimum number of elements across the diameter. Such suitable discretizations are obtained by evaluating the curvature of the vessel walls (which exist as a triangulation), and then using this information to adaptively refine and specify element sizes on a background grid that defines the spatial variation of element size in space [25–27].

2.2. Stent modeling

In order to simulate the flow of blood inside the parent artery and the aneurysm in the presence of a stent, a finite element mesh needs to be generated. Past experience (as well as that of colleagues

Copyright © 2007 John Wiley & Sons, Ltd.

DOI: 10.1002/fld

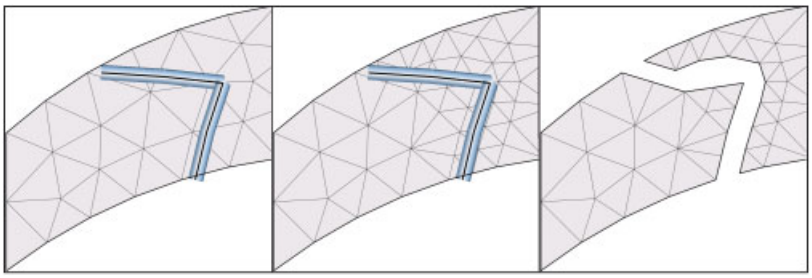

Figure 2. Modeling of vessels using the body-fitted approach and stents using the embedded approach: the body-fitted grid and the embedded stent (left), mesh refinement around the device (center) and the first-order approximation of the stent (right).

who have attempted the same) has shown that the creation of a body-conforming mesh for patient-specific models containing endovascular devices is very difficult. In some cases it may even be impossible with today's tools. The main difficulty stems from the fact that a body-conforming mesh requires a watertight assembly of analytical or discrete patches to describe the surface of the computational domain. Creating this watertight geometrical model can be very tedious, even for stents with relatively simple geometries. In contrast, in the case of the embedded approach the description of the embedded device is independent from that of the vessel, i.e. the geometrical modeling of the vessel and the stent has been decoupled. Thus, in this work, a hybrid body-fitted (for the vessel) and embedded (for the stent) approach is used as the best solution [22]. This approach consists in the following steps: (a) generate a body-conforming grid for the artery, (b) create a geometrical representation of the stent in its deployed state, (c) find the mesh elements cut by the stent, (d) adaptively refine these elements, and (e) eliminate the cut element edges from the flow calculation imposing no-slip boundary conditions at the cut points (see Section 2.4). This process is schematically illustrated in Figure 2. More details of these steps are provided in what follows.

Two basic options can be used to represent the geometry of the stents: (a) generate a surface triangulation (explicit surface definition), or (b) generate a series of overlapping spheres to define the stent geometry (implicit surface definition). In the latter approach, the distance between the spheres can be adjusted to represent the stent to any degree of accuracy. The two approaches are illustrated in Figure 3. Since the geometry of the stent is only used to determine the elements of the computational grids that are cut by the stent surface, these two approaches differ only in the way that the intersection between the stent wire surfaces and the computational grid is computed. In the former approach this requires computing the intersections between triangles of the stent surface and edges of the computational tetrahedral mesh. In contrast, the latter approach requires intersections between these edges and the spheres representing the stent, which is simpler to implement.

2.3. Stent deployment

Irrespective of the method chosen to represent the stent geometry, a method to deploy a given stent into a patient-specific vascular model is necessary. In this work we use the following approach. First, the skeleton of the parent vessel is extracted using a previously developed algorithm [28]. Then, a cylindrical surface is generated along this skeleton. This surface is considered as an elastic

Copyright © 2007 John Wiley & Sons, Ltd.

DOI: 10.1002/fld

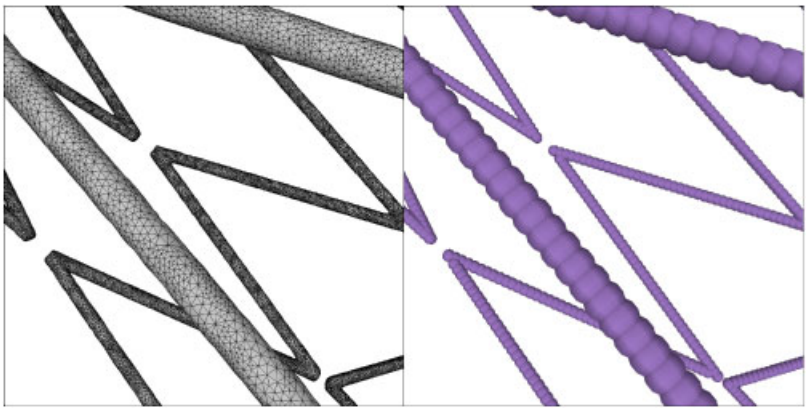

Figure 3. Stent geometry represented as a surface triangulation (left) and a series of overlapping spheres (right).

material and is deformed under the influence of internal smoothing forces and external attractive forces to the vessel wall. This is achieved by solving the elasticity equations on the triangulated cylindrical surface:

$$\rho \dot{V}_i = \frac{\partial \sigma_{ij}}{\partial x_j} + \rho b_i \tag{1}$$

This equation is solved using finite elements. In variational form this equation is

$$\int_{\Omega_t} \rho \dot{V}_i w_i \, \mathrm{d}\Omega_t = -\int_{\Omega_t} \varepsilon(w)_{ij} \sigma_{ij} \, \mathrm{d}\Omega_t + \int_{\Omega_t} \rho b_i w_i \, \mathrm{d}\Omega_t + \int_{\Gamma_t} w_i t_i \, \mathrm{d}\Gamma_t \tag{2}$$

The first term on the left-hand side represents the acceleration. The first term on the right-hand side constitutes the internal forces, f_{int}, and the last two terms are external forces, f_{ext}. Equation (2) is solved using the Newmark algorithm [29, 30], which can be written as

$$d_{n+1} = d_n + \Delta t v_n + \frac{\Delta t^2}{2} [(1 - 2\beta) a_n + 2\beta a_{n+1}] \tag{3}$$

$$v_{n+1} = v_n + \Delta t [(1 - \gamma) a_n + \gamma a_{n+1}] \tag{4}$$

In the first stage a cylindrical surface which is made up of shell elements is at the center of the parent vessel, as time progresses a combination of the f_{int} and f_{ext} is used to pull the cylinder to the vessel walls. Since the vessel walls are non-uniform the deformation of the cylindrical surface is also non-uniform. The deformation process is performed interactively and stopped when most of the points on the cylindrical surface are on the vessel wall. When a point crosses the vessel wall, i.e. its normal distance changes sign, it is projected onto the wall and fixed. Then, different stent designs can be mapped onto this cylindrical surface. The stent designs are drawn as a collection of connected lines with appropriate thickness. These designs are used to generate beads of overlapping spheres along the lines and mapped to the surface of the deformed cylinder in order to obtain the final stent model in the deployed state. The procedure to deploy a stent into a patient-specific vascular model of a cerebral aneurysm is illustrated in Figure 4. This figure

Copyright © 2007 John Wiley & Sons, Ltd.

DOI: 10.1002/fld

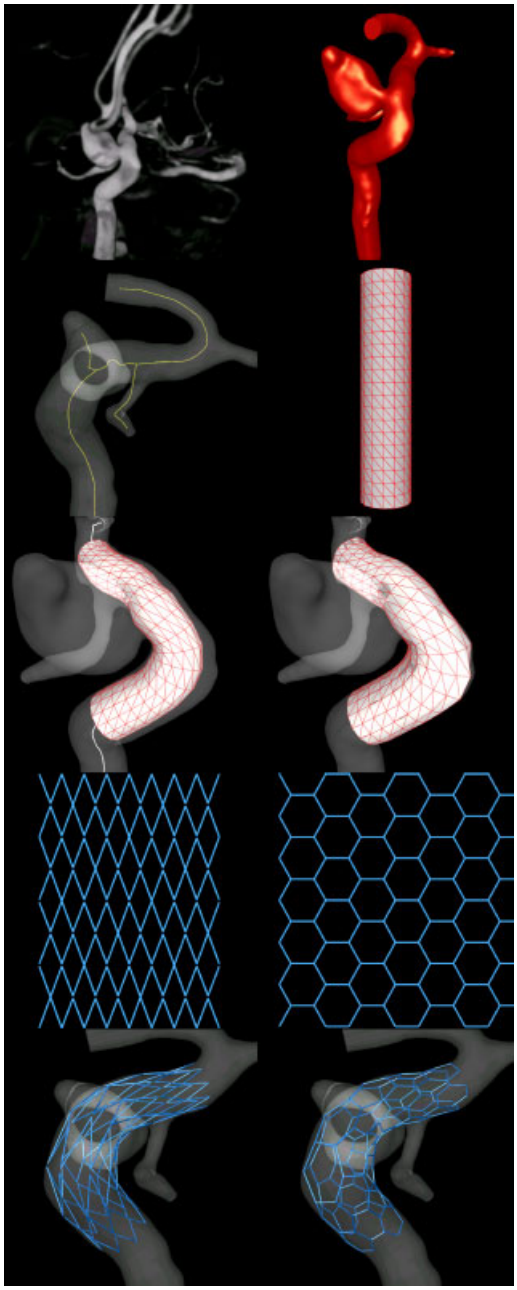

Figure 4. Steps followed in the vascular deployment of stents: the 3D rotational angiography image (top row, left column), reconstructed anatomical model (top row, right column), construction of the skeleton of the vascular model (second row, left column), initial cylindrical surface (second row, right column), cylindrical surface in the vessel skeleton (third row, left column), final cylindrical surface (third row, right column), two stent designs (fourth row) and the stents after deployment (fifth row).

Copyright © 2007 John Wiley & Sons, Ltd.

DOI: 10.1002/fld

shows the 3D RA image, the reconstructed anatomical model, the construction of the skeleton of the vascular model, the initial cylindrical surface, the cylindrical surface along the vessel skeleton, the final cylindrical surface (after deformation toward the vessel walls), two stent designs and the two stents after deployment.

2.4. Hemodynamics modeling

In this paper, for simplicity and demonstration purposes, blood is considered as a Newtonian incompressible fluid.

It has been argued that in large arteries the rheological behavior of blood can reasonably be approximated by a Newtonian model [31]. In addition, hemodynamic analyses of cerebral aneurysm models with realistic anatomies using Newtonian and non-Newtonian approximations indicate that the main flow characteristics are not significantly affected by the viscosity model [22]. However, non-Newtonian effects can become important in the slow flows encountered in stented aneurysms. This issue deserves further investigation.

Under these assumptions, the governing equations are the unsteady Navier–Stokes equations in three dimensions [32]

$$\nabla \cdot v = 0 \tag{5}$$

$$\frac{\partial v}{\partial t} + v \cdot \nabla v = -\frac{1}{\rho} \nabla p + \nu \nabla^2 v \tag{6}$$

where v is the velocity, p the pressure, ρ the density and ν the kinematic viscosity. In the simulations, values of $\rho = 1.0\,\mathrm{g/cm^3}$ and $\nu = 0.04\,\mathrm{cm^2/s}$ were used. The first equation is the continuity equation while the second is the conservation of momentum equation. These equations are discretized in time using an implicit scheme of the following form:

$$\nabla \cdot v^{n+\theta} = 0 \tag{7}$$

$$\frac{v^{n+\theta} - v^n}{\theta \Delta t} + v^{n+\theta} \cdot \nabla v^{n+\theta} + \frac{1}{\rho} \nabla p^{n+\theta} = \nabla \nu \cdot \nabla v^{n+\theta} \tag{8}$$

The parameter θ selects the time integration scheme used in the simulation. If $\theta = 1$ the first-order backward Euler scheme is recovered while with $\theta = \frac{1}{2}$ the second-order Crank–Nicholson is obtained [29, 30, 33]. Moving the first term to the right-hand side, this scheme can be interpreted as the steady-state solution of the pseudo-time system:

$$\frac{\partial v^{n+\theta}}{\partial \tau} + v^{n+\theta} \cdot \nabla v^{n+\theta} + \frac{1}{\rho} \nabla p^{n+\theta} = \nabla \nu \cdot \nabla v^{n+\theta} - \frac{v^{n+\theta} - v^n}{\theta \Delta t} \tag{9}$$

This is similar to the original Navier–Stokes equation but with a source term on the right-hand side. The solution is then advanced in time by solving a steady-state problem in pseudo-time τ at each time step. A linear (tetrahedral) finite element discretization of space is used. The discrete system is obtained *via* the Galerkin weighted residual method. For efficiency purposes, the data structures required are switched from element based to edge based. The resulting discrete system is of the following form:

$$K^{ij} \Delta u^j = \sum_{ij_\Omega} C^{ij} (F_i + F_j) \tag{10}$$

Copyright © 2007 John Wiley & Sons, Ltd.

DOI: 10.1002/fld

where $K^{ij}, C^{ij}, F_i, \Delta u^i$ denote the implicit left-hand side matrix, the explicit right-hand side matrix entries, nodal fluxes and increments in the nodal unknowns. The numerical scheme becomes unstable when a Galerkin finite element approximation is done on the advection terms. Therefore, an edge-based upwind finite element approximation is employed to discretize the equations in space [27, 33]. The coupled system is solved iteratively using a fractional step scheme with lower–upper symmetric Gauss–Seidel (LU-SGS) relaxation for the advection parts and a preconditioned conjugate gradient solver for the pseudo-Laplacian of the pressure. The scheme has been optimized over many years, and has been detailed elsewhere [22, 33].

2.5. Boundary conditions

In this work the vessel walls were assumed rigid for simplicity. Although vessel wall compliance can have a significant effect on hemodynamic variables, previous sensitivity analyses incorporating vessel deformations measured with dynamic imaging techniques suggest that the major flow characteristics such as size and location of the flow impaction zone or the complexity and stability of the intra-aneurysmal flow patterns are not fundamentally changed [34]. These macroscopic flow characteristics have been identified as possible predictors of aneurysm rupture [35], and are, therefore, important for evaluating the hemodynamic changes induced by different endovascular devices. No-slip boundary conditions are prescribed at the vessel walls, which for rigid walls becomes $v = 0$ at the vessel wall.

For pulsatile flow calculations, the inflow velocity is obtained as a superposition of Womersley profiles for each of the Fourier modes of the prescribed flow rate curve [36, 37]. This rate is obtained either from magnetic resonance measurements for patient-specific cases, or using typical patient data for generic cases. These boundary conditions assume fully developed flows and no secondary flows at the inlet boundaries. Some of our previous research has shown that if subject-specific models are truncated too close to the aneurysm neck, fully developed flow conditions can alter the inflow pattern into the aneurysm and the associated intra-aneurysmal hemodynamics [38]. However, these assumptions have less influence if the anatomical models include longer upstream portions of the parent artery allowing for the development of appropriate secondary flows due to the curvature and tortuosity of the parent vessel.

Traction-free (essentially prescribed pressure) or resistance ($p = R \cdot q$, R, q denoting resistance and mass flux, respectively) boundary conditions are prescribed at the model outflow boundaries. The resistance R can be estimated from a vascular bed model [39]. For the results shown below, only one exit required a pressure boundary condition, so there is no difference between the two conditions.

2.6. Treatment of embedded objects

The treatment of surfaces that are not body conforming and thus embedded into a larger flowfield domain/mesh has been the subject of much research [40–56]. In the literature several names have been coined to describe essentially the same procedure: embedded mesh, fictitious domain, immersed boundary, immersed body, Cartesian method, etc. In the present case, the *kinematic* boundary conditions are enforced in the vicinity of embedded objects. In other words, the velocity is set to zero at the nodes of cut-edges. As the basic flow solver is edge based, two immediate options appear: remove (first order) or duplicate (second order) the edges that are crossing embedded objects. Figure 5 illustrates the basic difference between these approaches. Computational structural

Copyright © 2007 John Wiley & Sons, Ltd.

DOI: 10.1002/fld

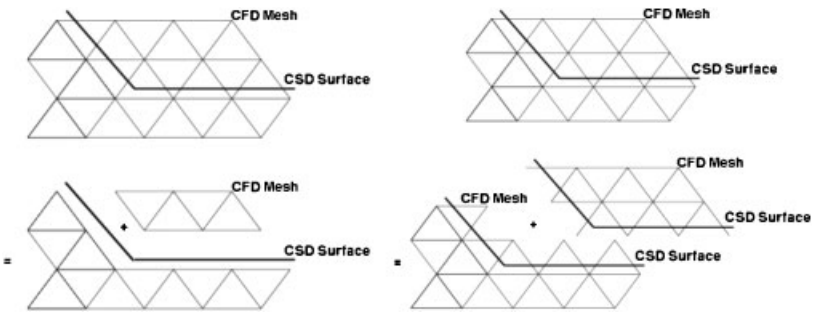

Figure 5. First- and second-order treatment of embedded surfaces.

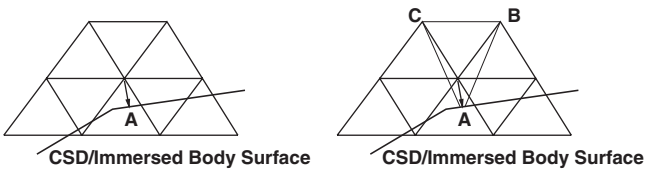

Figure 6. Extrapolation of velocity.

dynamics (CSD) denotes the surface of the embedded object or structure. Note that in both cases the treatment of infinitely thin surfaces with fluid on both sides is straightforward.

For the first-order scheme the main steps required are: elimination of edges crossing the embedded surface; formation of additional boundary coefficients to achieve flux balance (as edges have disappeared); and application of boundary conditions for the end points of the crossed edges based on the normals and velocities of the embedded surfaces.

For the second-order scheme, the steps are: duplication of edges crossing the embedded surface; duplication of end points of crossed edges; and application of boundary conditions for the end points of the crossed edges based on the normals and velocities of the embedded surface.

Note that many of the capabilities required for either scheme are the same: identification of crossed edges, application of new boundary conditions and reordering of arrays.

These procedures have been described in more detail in [22, 57, 58]. The first-order scheme may be improved by extrapolating the velocity from the surface with field information. The location where the flow velocity is equal to the surface velocity is the surface itself, and not the closest boundary point. As shown in Figure 6, for each boundary point the closest point on the CSD face is found. Then, two (three) neighboring field (i.e. non-boundary) points are found and a triangular (tetrahedral) element that contains the boundary point is formed. The velocity imposed at the field point is then found by interpolation. In this way, the boundary velocity 'lags' the field velocities by one iteration (for iterative implicit schemes) or time step (for explicit schemes).

In order to increase the overall efficiency of the algorithm, points that are completely surrounded by cut-edges are deactivated and removed from the flow calculation. For more information on the unstructured grid embedding technique used, the reader is referred to [22, 57, 58].

Copyright © 2007 John Wiley & Sons, Ltd.

DOI: 10.1002/fld

3. RESULTS

3.1. Flow past a cylinder

First, the methodology was tested on a flow around a circular cylinder under steady flow conditions. This test was done to compare the results obtained with the embedded and body-fitted methods and experimental data from the literature. The cylinder was 0.01 cm in diameter, which is typical of the diameter of stent wire. This cylinder was placed in a box of dimensions $1.0\,\text{cm} \times 0.5\,\text{cm} \times 0.01\,\text{cm}$. The origin is at the center of the cylinder, with the x-axis from left to right and the y-axis in the vertical direction. A body-conforming mesh was generated with a resolution of 0.02 cm in the far field and 0.00075 cm near the surface of the cylinder. The mesh consisted approximately $365K$ elements (see Figure 7, left panel). Steady-state simulations were carried out using a Reynolds number of $Re = 25$. This is a typical value for the Reynolds number of a stent in a cerebral artery. This can be calculated with the assumptions that for blood $\rho = 1.0\,\text{g/cm}^3$, $\mu = 0.04\,\text{P}$, and in cerebral arteries blood velocity $v = 100\,\text{cm/s}$ and the stent wire has a diameter of $d = 0.01\,\text{cm}$. Uniform velocity profile was prescribed at the inflow, traction-free boundary conditions at the outlet and no-penetration boundary conditions were used in the walls of the box. The flow direction is from left to right.

For the embedded approach, an initial uniform mesh without the cylinder was created with a resolution of 0.01 cm. This grid contained approximately $36K$ elements. Then a cylindrical surface was embedded in this grid and adaptively refined around it. The mesh was refined with four, five, six and seven levels of refinement obtaining approximately $92K$, $242K$, $822K$ and $3M$ elements, respectively. Computational fluid dynamics (CFD) simulations were performed for these grids using the same conditions prescribed in body-fitted run. Figure 7 shows the details of the finite element grids. Since stents are represented as a sequence of overlapping spheres, similar set of runs were performed by approximating the cylinder with 50 overlapping spheres.

Figure 8 shows the contour of velocity magnitude obtained with the body-fitted grid (left) and with the embedding approach after four (center) and six (right) levels of refinement. The results obtained for the embedded technique show good correlation with the body-fitted results. Table I shows the value of the drag coefficient and its percentage error in brackets for the body-fitted and embedded simulations, in comparison with the experimental value [59]. The results show that the error decreases with the increase in levels of refinement.

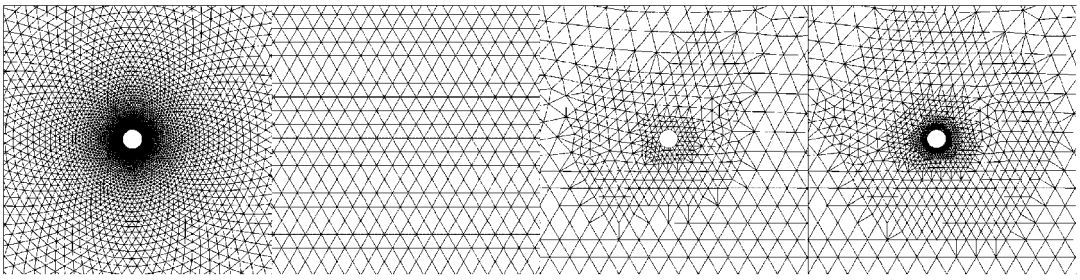

Figure 7. Grids used for the flow simulation. From left to right: body-fitted grid, uniform mesh with no refinement, mesh with two levels of refinement and mesh after four levels of refinement.

Copyright © 2007 John Wiley & Sons, Ltd.

DOI: 10.1002/fld

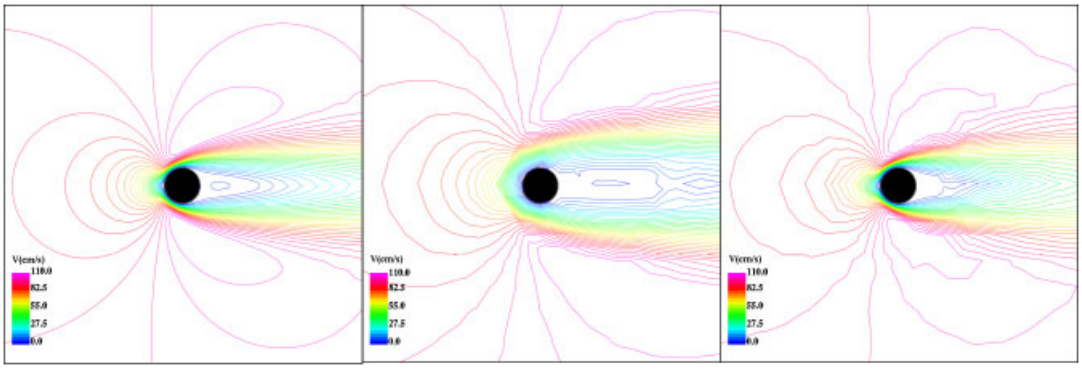

Figure 8. Velocity contours for the body-fitted grid (left column), the embedded grid with four levels of refinement (center column) and the embedded grid with six levels of refinement (right column).

Table I. Drag coefficient for $Re = 25$.

		Level 4	Level 5	Level 6	Level 7
Experimental	1.8597				
Body-fitted	1.8488				
	(−0.6%)				
Embedded surface triangulation		1.6851	1.7439	1.809	1.847
		(−9.4%)	(−6.2%)	(−2.7%)	(−0.7%)
Embedded overlapping spheres		1.607	1.7247	1.8147	1.8773
		(−13.6%)	(−7.3%)	(−2.4%)	(1.0%)

These results show that for the low Reynolds numbers usually encountered in blood flows with stents, the embedded technique produces good results. This example also shows that as the level of refinement is increased, the solution becomes more accurate and the drag coefficient converges to the experimental value. Since the mesh refinement is entirely automatic, no extra modeling work is needed to achieve higher levels of accuracy. This is what makes the embedded approach very attractive.

3.2. Idealized stented aneurysm

In this example, an idealized aneurysm model was constructed by merging the triangulations of a cylinder and a sphere. The parent vessel was modeled as a cylinder of 0.35 cm diameter. The spherical aneurysm was modeled as a sphere of radius 0.466 cm displaced 0.4 cm from the axis of the parent vessel. A stent was modeled with 12 intersecting helices of 0.01 cm in diameter and 0.5 cm long. The helices were distributed along the circumference of the parent vessel with alternating directions of rotation, and one turn from one end to the other. The body-fitted and the embedded techniques were used to grid this idealized stented aneurysm. The body-fitted grid was constructed as follows. First, a vascular model was created by merging the surface triangulations of the parent vessel (cylinder) and the aneurysm (sphere). Secondly, a geometrical model of the stent was created by generating independent triangulations along each helical wire and then fusing

Copyright © 2007 John Wiley & Sons, Ltd.

DOI: 10.1002/fld

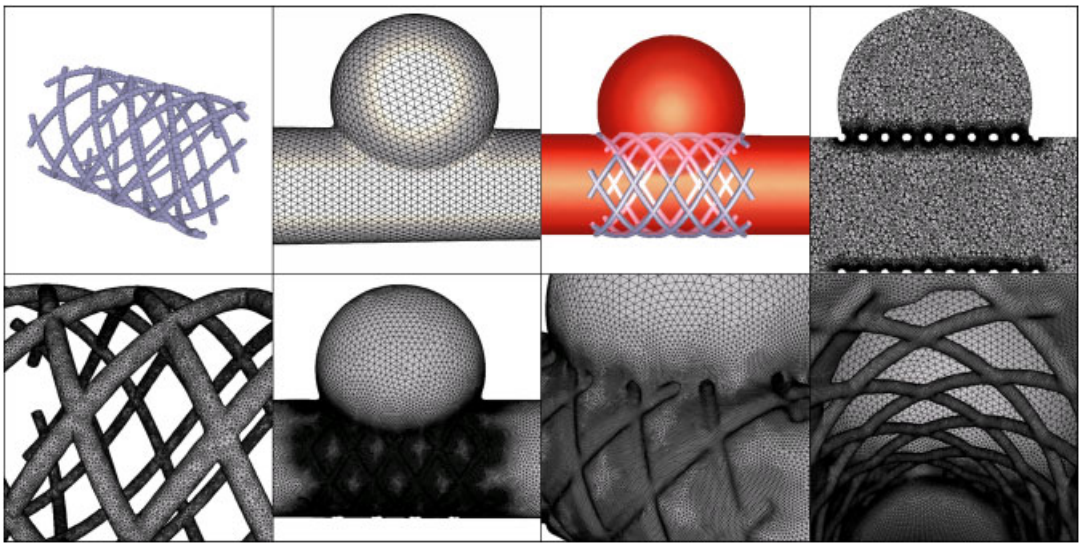

Figure 9. Embedded grid model (top row) and body-fitted model (bottom row).

them with the same surface-merging algorithm. Then, the final geometrical model was created by fusing (subtracting) the triangulations of the vascular model and the stent. This geometrical model was used to generate a finite element grid, that contained approximately 10 M elements. For the embedded approach the vascular model (without the stent) was meshed, resulting in an initial grid of 763 K elements. This grid was then refined one, two and three levels, resulting in a total of 1.2 M, 2.85 M and 8.5 M elements, respectively. Figure 9 shows the geometry of the model and the grids.

Flow calculations were carried out under steady flow conditions, corresponding to the aneurysm before and after stenting using the body-fitted and embedded approaches. A parabolic velocity distribution corresponding to a total flow rate of $Q = 4.78\,\mathrm{ml/s}$ was prescribed at the model entrance and traction-free boundary conditions at the outlet. As the main tube is straight, a parabolic velocity profile was deemed appropriate. Figure 10 shows the velocity contours (left column) and streamlines (right column) before stenting (top row) and after stenting using the body-fitted (center row) and embedded (bottom row) techniques. It can be seen that the results obtained with body-fitted and embedded grid approaches are similar. These visualizations also show the alterations in the aneurysmal flow pattern caused by the stent. Before stenting the inflow zone is located at the distal part of the neck (left in Figure 10) and the flow rotates in the clockwise direction inside the aneurysm. After stenting, the inflow zone is located at the proximal end of the neck (right in Figure 10) and the intra-aneurysmal flow rotates in the counter-clockwise direction. This observation is consistent with observations made by Lieber *et al*. using *in vitro* models and particle image velocimetry techniques [60].

In order to further compare the solutions obtained with the body-fitted and embedded grids the velocity magnitude was plotted along three lines placed inside the aneurysm parallel to the neck and at different depths. Figure 11 shows the plots of the velocity magnitude along these lines. The location of these lines inside the aneurysms is also shown in Figure 11. These results also

Copyright © 2007 John Wiley & Sons, Ltd.

DOI: 10.1002/fld

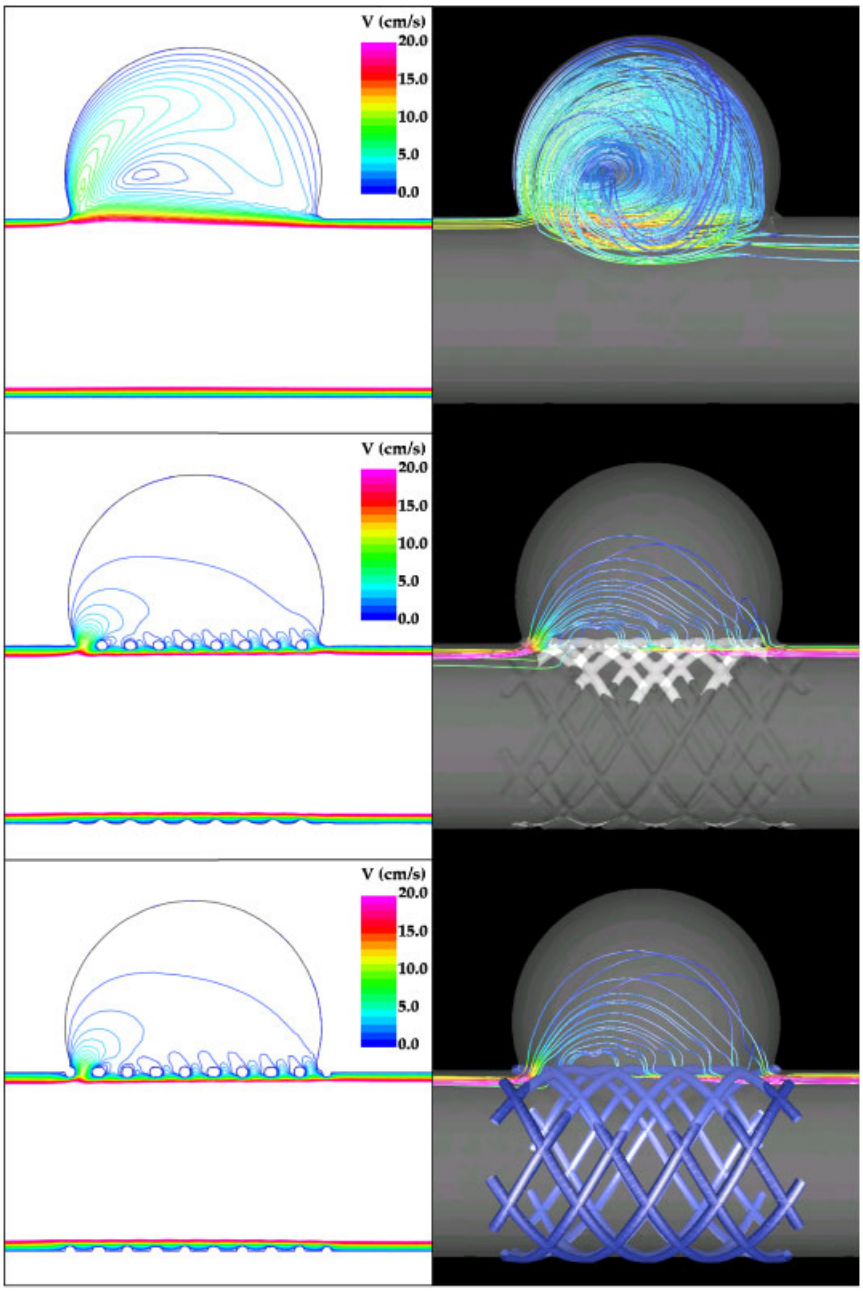

Figure 10. Velocity contours (left column) and streamlines (right column), before stenting (top row), body-fitted (middle row) and embedded (bottom row).

Copyright © 2007 John Wiley & Sons, Ltd.

DOI: 10.1002/fld

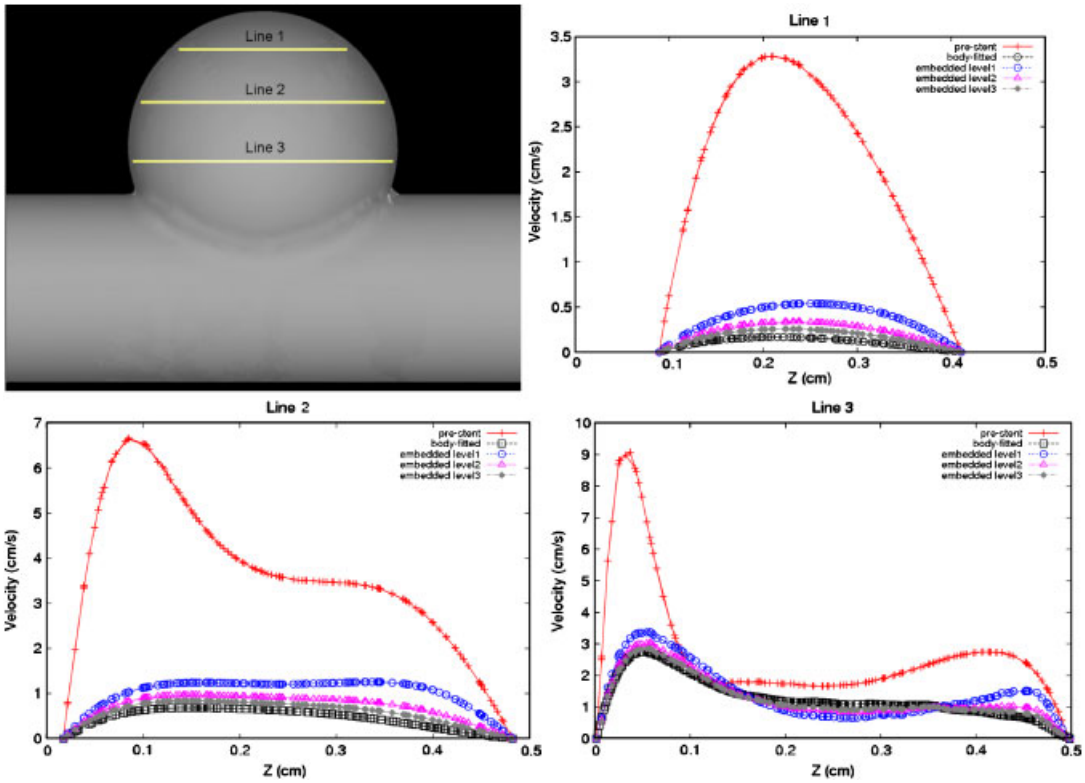

Figure 11. Position of the lines and their respective plots.

Table II. Comparison of velocity reduction between body-fitted and embedded grid methods.

Line	Pre-stenting	Body-fitted	Embedded level 1	Embedded level 2	Embedded level 3
1	3.26 cm/s	0.95	0.85 (11%)	0.9 (5%)	0.92 (3%)
2	6.54 cm/s	0.9	0.83 (8%)	0.86 (4%)	0.88 (2%)
3	9.1 cm/s	0.72	0.65 (10%)	0.69 (4%)	0.71 (1%)

show a good agreement between the two approaches and that the embedded grids yield results that converge to the body-fitted result as the levels of refinement are increased. The reduction in the maximum velocity along each of these lines obtained with the different methods are listed in Table II. The left column of this table lists the maximum values of the velocity along each line. The other columns list the factor by which this maximum velocity is reduced, as computed by the different methods. The percent values in parentheses are the relative errors between the velocity reduction factors with respect to the one computed with the body-fitted grid. This table indicates

Copyright © 2007 John Wiley & Sons, Ltd.

DOI: 10.1002/fld

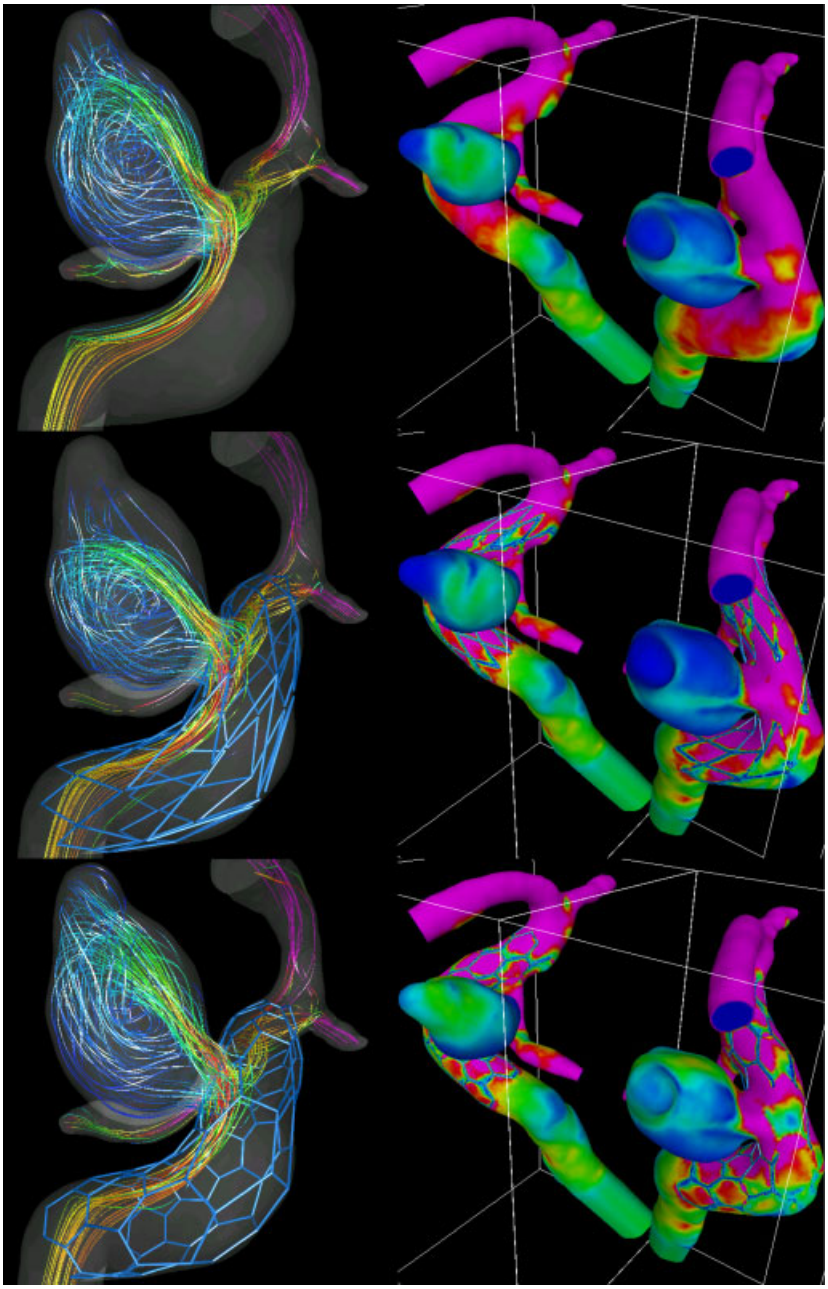

Figure 12. Streamlines (left column) and wall shear stress (right column) for the aneurysm before stenting (top row), with stent 1 (center row) and with stent 2 (bottom row). The wall shear stress distributions are rendered from two perpendicular viewpoints using a mirror.

Copyright © 2007 John Wiley & Sons, Ltd.

DOI: 10.1002/fld

that with only two levels of refinement, the velocity reduction after stenting was predicted within 5% of the prediction made by the body-fitted method.

3.3. Patient-specific model

This example demonstrates the use of the mesh embedded technique to calculate the flow field in a realistic or patient-specific model of a cerebral aneurysm with stents of different designs. The vascular model was constructed from 3DRA images obtained during intravascular injection of contrast agent as explained before. The first stent (stent 1) comprises rhomboidal cells similar to the Neuroform stent (Boston Scientific, Inc.). The second stent (stent 2) was constructed with hexagonal cells with the same amount of metal as the first stent. A total of three CFD simulations were carried out, corresponding to pre-stenting and after stenting with each of the two stents. In these calculations, physiologic pulsatile flow rates derived from phase-contrast MR measurements in normal subjects were described at the inlet of the internal carotid artery [61]. Traction-free boundary conditions were imposed at the model outlets.

Figure 12 shows visualizations of the hemodynamics (streamlines at peak systole and wall shear stress) before and after stent deployment. In the wall shear stress visualizations, a mirror was used to make both sides of the aneurysm visible. In comparison with the flow without the stent, the first stent design (middle row) diverts the inflow jet toward the center of the aneurysm dome, and reduces the wall shear stress in the body of the aneurysm. In contrast, the second stent design does not alter the flow pattern significantly. This example illustrates how the methodology can be used to understand the changes in the hemodynamics produced by different stents. This can be useful for selecting the best stent for a given aneurysm.

4. CONCLUSIONS

A methodology to simulate blood flows in patient-specific models with stents that combines body-fitted and embedded grids has been developed and evaluated. This approach to a very large extent reduces the hardship associated with just using the body-conforming technique to mesh the parent vessel and around the endovascular devices. This is so because the mesh refinement and embedding steps are done in a fully automated way in a few minutes, while the generation of body-conforming grids can be a tedious manual process that can take from hours to weeks, depending on the geometric complexity of the problem. The methodology was evaluated with the flow past a circular cylinder and an idealized stented aneurysm. The results obtained were in close agreement with body-fitted computations and experimental results. These results also show that quantities such as the reduction in intra-aneurysmal flow velocity after stenting can be accurately calculated with the embedding approach with a relatively small number of mesh refinement levels.

A stent deployment algorithm was presented and demonstrated in a 'virtual stenting' simulation with a patient-specific anatomical model and two stent designs. This method represents a first attempt at modeling the stent geometry after deployment, and it can be used as the initial configuration for more complex models accounting for the material properties of the stent and the vessel wall. The significance of this work is that these techniques can potentially be used to select the best available stent to treat a given aneurysm. However, it is still not well understood how to best evaluate the relative performance of different stents.

Copyright © 2007 John Wiley & Sons, Ltd.

DOI: 10.1002/fld

In conclusion, this work shows that adaptive unstructured embedded grid approaches can be used for patient-specific 'virtual stenting' simulations in order to predict the alterations of the aneurysmal hemodynamics caused by the implantation of a stent. Furthermore, the results seem to indicate that the selection of the 'best' stent may be patient-specific because different anatomical characteristics can lead to very different flow patterns and, therefore, to different optimal stent designs for reducing the flow into each particular aneurysm.

ACKNOWLEDGEMENTS

This work was partially supported by a grant from Philips Medical Systems. It is also a pleasure to acknowledge Dr Daniel A. Rüfenatch from University Hospital in Geneva for interesting ideas, discussions and encouragement.

REFERENCES

1. Stehbens A. Intracranial arterial aneurysms. *Pathology of the Cerebral Blood Vessels*. CV Mosby: St. Louis, MO, 1972; 351–470.
2. Linn F, Rinkel G, Algra A, van Gijn J. Incidence of subarachnoid hemorrhage: role of region, year, and rate of computed tomography: a meta-analysis. *Stroke* 1996; **27**(4):625–629.
3. Foutrakis G, Yonas H, Selabassi R. Saccular aneurysm formation in curved and bifurcation arteries. *American Journal of Neuroradiology* 1999; **20**:1309–1317.
4. Weir B. Unruptured intracranial aneurysms: a review. *Journal of Neurosurgery* 2002; **96**:3–42.
5. Tomasello F, D'Avella D, Salpietro F, Longo M. Asumptomatic aneurysms. Literature metanalysis and indications for treatment. *Journal of Neurosurgery* 1998; **42**(1):47–51.
6. Winn H, Jane J, Taylor J, Kaiser D, Britz G. Detection of asymptomatic incidental aneurysms: review of 4568 arteriograms. *Journal of Neurosurgery* 2002; **96**(1):43–49.
7. Kaminogo M, Yonekura M, Shibata S. Incidence and outcome of multiple intracranial aneurysms in a defined population. *Stroke* 2003; **34**(1):16–21.
8. Ringer A, Lopes D, Boulos A, Guterman L, Hopkins L. Current techniques for endovascular treatment of intracranial aneurysms. *Seminar in Cerebrovascular Diseases and Stroke* 2001; **1**(1).
9. Lylyk P, Ferrario A, Pasbon B, Miranda C, Doroszuk G. Buenos Aires experience with the Neuroform self-expanding stent for the treatment of intracranial aneurysms. *Journal of Neurosurgery* 2005; **102**(2):235–241.
10. Lövbald KO, Yilmaz H, Chouiter A, Ruiz DSM, Abdo G, Bijlenga P, Tribolet N, Rüfenacht DA. Intracranial aneurysm stenting: follow-up with MR angiography. *Journal of Magnetic Resonance Imaging* 2006; **24**:418–422.
11. Szikora I, Berentei Z, Kulcsar Z, Barath K, Berez A, Bose A, Nyary I. Endovascular treatment of intracranial aneurysms with parent vessel reconstruction using balloon and self expandable stents. *Acta Neurochirurgica* 2006; **148**:711–723.
12. Ohta M, Wetzel SG, Dantan P, Bachelet C, Lovbald KO, Yilmaz H, Flaud P, Rüfenacht DA. Rheological changes after stenting of a cerebral aneurysm: a finite element modeling approach. *Cardiovascular and Interventional Radiology* 2005; **28**:768–772.
13. Yu SCM, Zhao JB. A steady flow analysis on the stented and non-stented sidewall aneurysm models. *Medical Engineering and Physics* 1999; **21**:133–141.
14. Wakhloo AK, Leiber BB. Alteration of hemodynamics in aneurysm models by stenting: influence of stent porosity. *Annals of Biomedical Engineering* 1997; **25**:460–469.
15. Barath K, Cassot F, Fasel JH. Influence of stent properties on the alteration of cerebral intra-aneurysmal hemodynamics: flow quantification in elastic sidewall aneurysm models. *Neurological Research* 2005; **27**: 120–128.
16. Jou LD, Quick CM, Young WL, Lawton MT, Higashida R, Martin A, Saloner D. Computational approach to quantify hemodynamic forces in giant cerebral aneurysms. *American Journal of Neuroradiology* 2004; **24**(9): 1804–1810.
17. Steinman D, Milner J, Norley C, Lownie S, Holdworth D. Image-based computational simulation of flow dynamics in a giant intracranial aneurysm. *American Journal of Neuroradiology* 2003; **24**(4):559–566.

Copyright © 2007 John Wiley & Sons, Ltd.

DOI: 10.1002/fld

18. Cebral JR, Hernandez M, Frangi AF. Computational analysis of blood flow dynamics in cerebral aneurysms from cta and 3d rotational angiography image data. *Proceedings of the International Congress on Computational Bioengineering*, Zaragoza, Spain, vol. 1, September 2003; 191–198.
19. Cebral JR, Hernandez M, Frangi AF, Putman CM, Pergolizzi M, Burgess JE. Subject-specific modeling of intracranial aneurysms. *SPIE Medical Imaging 2004*, San Diego, CA, vol. 5369, February 2004; 319–327.
20. Cebral JR, Castro MA, Burgess JE, Putman CM. Cerebral aneurysm hemodynamics modeling from 3d rotational angiography. *Proceedings of the IEEE Symposium on Biomedical Imaging* (*ISBI* 2004), Arlington, VA, April 2004; 944–947.
21. Löhner R, Baum J, Mestreau E, Sharov D. Adaptive embedded unstructured grid methods. *International Journal for Numerical Methods in Engineering* 2003; **60**:641–660.
22. Cebral JR, Löhner R. Efficient simulation of blood flow past complex endovascular devices using an adaptive embedding technique. *IEEE Transactions on Medical Imaging*, Special Issue on Vascular Imaging 2005; **24**(4): 457–467.
23. Cebral J, Löhner R, Choyke P, Yim P. Merging of intersecting triangulations for finite element modeling. *Journal of Biomechanics* 2001; **34**:815–819.
24. Cebral JR, Löhner R. From medical images to anatomically accurate finite element grids. *International Journal for Numerical Methods in Engineering* 2001; **51**:985–1008.
25. Löhner R. Regridding surface triangulations. *Journal of Computational Physics* 1996; **126**:1–10.
26. Löhner R. Automatic unstructured grid generators. *Finite Elements in Analysis and Design* 1997; **25**(1–2):111–134.
27. Löhner R. *Applied CFD Techniques*. Wiley: New York, 2001.
28. Cebral JR, Löhner R. Flow visualization on unstructured grids using geometrical cuts, vortex detection and shock surfaces. *AIAA-01-0915*, 2001.
29. Zienkiewicz OC, Taylor R. *The Finite Element Method*. McGraw-Hill: New York, 1988.
30. Hughes TR. *The Finite Element Method*: *Linear Static and Dynamic Finite Element Analysis*. Dover: New York, 2000.
31. Leuprecht A, Perktold K. Computer simulation of non-Newtonian effects on blood flow in large arteries. *Computer Methods in Biomechanics and Biomedical Engineering* 2001; **4**(2):149–163.
32. Mazumdar J. *Biofluid Mechanics*. World Scientific: Singapore, 1992.
33. Löhner R, Yang C, Cebral JR, Soto O, Camelli F, Waltz J. Improving the speed and accuracy of projection-type incompressible flow solvers. *Computer Methods in Applied Mechanics and Engineering* 2006; **195**(23–24): 3087–3109.
34. Dempere-Marco L, Oubel E, Castro MA, Putman CM, Frangi A, Cebral JC. *Estimation of Wall Motion in Intracranial Aneurysms and its Effect on Hemodynamic Patterns*. Lecture Notes in Computer Science, vol. 4191. Springer: Berlin, 2006; 438–445.
35. Cebral JR, Castro MA, Burgess JE, Pergolizzi RS, Sheridan MJ, Putman CM. Characterization of cerebral aneurysms for assessing risk of rupture by using patient-specific computational hemodynamics models. *American Journal of Neuroradiology* 2005; **26**(10):2550–2559.
36. Taylor C, Hughes T, Zarins C. Finite element modeling of blood flow in arteries. *Computer Methods in Applied Mechanics and Engineering* 1998; **158**:155–196.
37. Cebral JR, Yim P, Löhner R, Soto O, Choyke P. Blood flow modeling in carotid arteries using computational fluid dynamics and magnetic resonance imaging. *Academic Radiology* 2002; **9**:1286–1299.
38. Castro MA, Putman CM, Cebral JR. Patient-specific computational modeling of intracranial aneurysms: effects of parent artery segmentation on intra-aneurysmal hemodynamics. *American Journal of Neuroradiology* 2006; **27**(8):1703–1709.
39. Löhner R, Cebral JR, Soto OA, Yim, P, Burgess JE. Applications of patient-specific CFD in medicine and life sciences. *International Journal for Numerical Methods in Fluids* 2003; **43**:637–650.
40. Clarke DK, Hassan HA, Salas MD. Euler calculations for multielement airfoils using Cartesian grids. *AIAA*-85-0291, 1985.
41. de Zeeuw D, Powell K. An adaptively-refined Cartesian mesh solver for the Euler equations. *AIAA-91-1542*, 1991.
42. Melton JE, Berger MJ, Aftosmis MJ. 3-D applications of a Cartesian grid Euler method. *AIAA-93-0853-CP*, 1993.
43. Quirk JJ. A Cartesian grid approach with hierarchical refinement for compressible flows. *NASA CR-194938, ICASE Report No. 94-51*, 1994.
44. Karman SL. SPLITFLOW: a 3-D unstructured Cartesian/prismatic grid CFD code for complex geometries. *AIAA-95-0343*, 1995.

Copyright © 2007 John Wiley & Sons, Ltd.

DOI: 10.1002/fld

45. Pember RB, Bell JB, Colella P, Crutchfield WY, Welcome ML. An adaptive Cartesian grid method for unsteady compressible flow in irregular regions. *Journal of Computational Physics* 1995; **120**:278–304.
46. Landsberg AM, Boris JP. The virtual cell embedding method: a simple approach for gridding complex geometries. *AIAA-97-1982*, 1997.
47. Turek S. *Efficient Solvers for Incompressible Flow Problems*. Springer Lecture Notes in Computational Science and Engineering, vol. 6. Springer: Berlin, 1999.
48. Mohd-Yusof J. Combined immersed-boundary/B-spline methods for simulations of flow in complex geometries. *CTR Annual Research Briefs*, NASA Ames Research Center/Stanford University, 1997; 317–327.
49. Glowinski R, Pan TW, Hesla TI, Joseph DD. A distributed Lagrange multiplier/ficticious domain method for particulate flows. *International Journal of Multiphase Flow* 1999; **25**(5):755–794.
50. Aftosmis MJ, Berger MJ, Adomavicius G. A parallel multilevel method for adaptively refined Cartesian grids with embedded boundaries. *AIAA-00-0808*, 2000.
51. LeVeque RJ, Calhoun D. Cartesian grid methods for fluid flow in complex geometries. In *Computational Modeling in Biological Fluid Dynamics*, Fauci LJ, Gueron S (eds). IMA Volumes in Mathematics and its Applications, vol. 124. Springer: Berlin, 2001; 117–143.
52. Dadone A, Grossman B. An immersed boundary methodology for inviscid flows on Cartesian grids. *AIAA-02-1059*, 2002.
53. Peskin CS. The immersed boundary method. *Acta Numerica* 2002; **11**:479–517.
54. Gilmanov A, Sotiropoulos F, Balaras E. A general reconstruction algorithm for simulating flows with complex 3D immersed boundaries on Cartesian grids. *Journal of Computational Physics* 2003; **191**(2):660–669.
55. Gilmanov A, Sotiropoulos F. A hybrid Cartesian/immersed boundary method for simulating flows with 3-D, geometrically complex moving objects. *Journal of Computational Physics* 2005; **207**:457–492.
56. Mittal R, Iaccarino G. Immersed boundary methods. *Annual Review of Fluid Mechanics* 2005; **37**:239–261.
57. Löhner R, Baum JD, Mestreau E, Sharov D, Charman C, Pelessone D. Adaptive embedded unstructured grid methods. *International Journal for Numerical Methods in Engineering* 2004; **60**:641–660.
58. Löhner R, Appanaboyina S, Cebral JR. Comparison of body-fitted, embedded and immersed solutions for low Reynolds-number flows. *AIAA-07-1296*, 2007.
59. Schlichting H, Gersten K. *Boundary Layer Theory* (8th revised edn). Springer: Berlin, 2000.
60. Lieber BB, Livescu V, Hopkins LN, Wakhloo AK. Particle image velocimetry assessment of stent design influence on intra-aneurysmal flow. *Annals of Biomedical Engineering* 2002; **30**:768–777.
61. Cebral JR, Castro MA, Soto OA, Löhner R, Alperin N. Blood-flow models of the circle of Willis from magnetic resonance data. *Journal of Engineering Mathematics* 2003; **47**:369–386.

Copyright © 2007 John Wiley & Sons, Ltd.

DOI: 10.1002/fld